



The cloudy atmospheric boundary layer over the subtropical South Atlantic Ocean: Airborne-spaceborne lidar observations and numerical simulations

Stéphanie Cosma-Averseng, Cyrille Flamant, Jacques Pelon, Stephen P. Palm,
Geary K. Schwemmer

► To cite this version:

Stéphanie Cosma-Averseng, Cyrille Flamant, Jacques Pelon, Stephen P. Palm, Geary K. Schwemmer. The cloudy atmospheric boundary layer over the subtropical South Atlantic Ocean: Airborne-spaceborne lidar observations and numerical simulations. *Journal of Geophysical Research: Atmospheres*, 2003, 108 (D7), <10.1029/2002JD002368>. <hal-04110036>

HAL Id: hal-04110036

<https://hal.science/hal-04110036v1>

Submitted on 5 Jun 2023

HAL is a multi-disciplinary open access archive for the deposit and dissemination of scientific research documents, whether they are published or not. The documents may come from teaching and research institutions in France or abroad, or from public or private research centers.

L'archive ouverte pluridisciplinaire **HAL**, est destinée au dépôt et à la diffusion de documents scientifiques de niveau recherche, publiés ou non, émanant des établissements d'enseignement et de recherche français ou étrangers, des laboratoires publics ou privés.



Copyright - All rights reserved

The cloudy atmospheric boundary layer over the subtropical South Atlantic Ocean: Airborne-spaceborne lidar observations and numerical simulations

Stéphanie Cosma-Averseng, Cyrille Flamant, and Jacques Pelon

Service d'Aéronomie, Institut Pierre-Simon Laplace, Université Pierre et Marie Curie, Paris, France

Stephen P. Palm

Science Systems and Applications, Inc., Lanham, Maryland, USA

Geary K. Schwemmer

Laboratory for Atmospheres, NASA Goddard Space Flight Center, Greenbelt, Maryland, USA

Received 25 March 2002; revised 9 September 2002; accepted 30 January 2003; published 12 April 2003.

[1] This paper focuses on the structure of the marine boundary layer in an convergence region between easterly (trade winds) and westerly flows, over the Subtropical South Atlantic Ocean on 15 September 1994 using an unprecedented combination of spaceborne and airborne lidar observations, airborne Radar Ocean Wave Spectrometer and dropsondes system, and three-dimensional modeling. Methodologies previously developed to determine the marine atmospheric boundary layer (MABL) depth and cloud top heights from airborne lidar measurements are successfully applied to spaceborne measurements. Nested numerical simulations have been performed in this case study. It is shown that the MABL structure in this region (observed with lidar and simulated) collapsed dramatically in connection with a marked decrease of wind speed and near-zero turbulent kinetic energy due to specific synoptic conditions. *INDEX TERMS:* 3307

Meteorology and Atmospheric Dynamics: Boundary layer processes; 3337 Meteorology and Atmospheric Dynamics: Numerical modeling and data assimilation; 3339 Meteorology and Atmospheric Dynamics: Ocean/atmosphere interactions (0312, 4504); 3394 Meteorology and Atmospheric Dynamics: Instruments and techniques; *KEYWORDS:* atmospheric boundary layer, subtropical South Atlantic Ocean, lidar, meso-NH numerical simulations, Lidar In-Space Technology Experiment

Citation: Cosma-Averseng, S., C. Flamant, J. Pelon, S. P. Palm, and G. K. Schwemmer, The cloudy atmospheric boundary layer over the subtropical South Atlantic Ocean: Airborne-spaceborne lidar observations and numerical simulations, *J. Geophys. Res.*, 108(D7), 4220, doi:10.1029/2002JD002368, 2003.

1. Introduction

[2] The marine atmospheric boundary layer (MABL) plays an important role in atmospheric dynamics and climate evolution as it controls the exchanges of heat, moisture and material between the surface and the free troposphere, which are key to convection initiation and cloud development.

[3] Accurate weather and climate prediction implies that global circulation models are able to correctly reproduce these exchanges as well as cloud formation. However, in subtropical regions of persistent marine stratocumulus, the cloud cover and the MABL structure are still not well represented [e.g., Grenier and Bretherton, 2001]. It is now well accepted that significant insight into the parameterization of convection, turbulence, and clouds processes will be gained through the association of high resolution numerical modeling and in-situ/remote-sensing observations.

[4] In recent years, numerical models of varying degrees of complexity have been developed, focusing on some of the above mentioned mechanisms in detail. At the same time, field experiments such as the First ISCCP Regional Experiment (FIRE) [Cox *et al.*, 1987] and the Atlantic Stratocumulus Transition Experiment (ASTEX) [Albrecht *et al.*, 1995] have been conducted to study the MABL processes involved in the life cycle of stratocumulus cloud decks southwest of the California Coast and in the region of the Azores, respectively. The high-quality data sets acquired during these field experiments have since been extensively used to improve the representation of stratocumulus in numerical models [e.g., Bretherton and Pincus, 1995; De Roode and Dyunkerke, 1997]. However, these field experiments offer limited observations in restricted areas. To date, no network-type observations are available over the oceans on a global scale, which means that MABL oriented analyses over the remote oceans might be usefully accomplished from space. Furthermore, such analyses require highly resolved measurements both on the horizontal and on the vertical. This cannot be achieved at present by

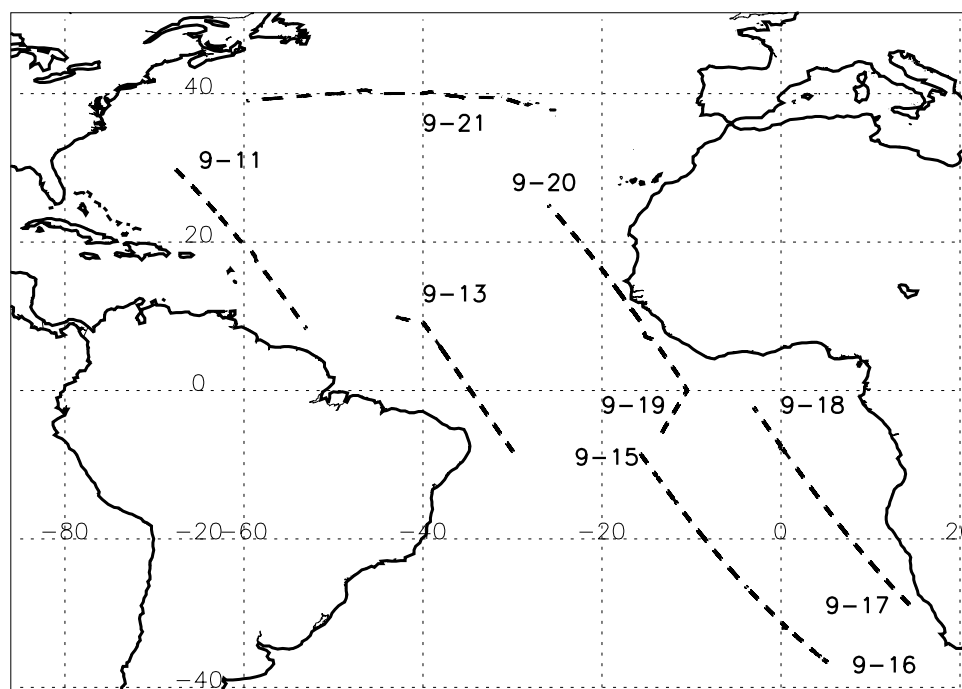


Figure 1. P-3B flight tracks for the five LITE underflights over the Atlantic Ocean. Dates are indicated in the vicinity of the tracks.

spaceborne passive instruments which only provide a two-dimensional coverage integrated over the vertical. However, it will soon be possible as the next generation of sounders, IASI (Infrared Atmospheric Sounding Interferometer) and AIRS (Atmospheric InfraRed Sounder), will provide vertically resolved (1 km) profiles of meteorological variables.

[5] At the present time, only lidar systems can provide this information on the vertical distribution of cloud and aerosol layers. Airborne and spaceborne lidars also offer the advantage of penetrating thin or broken clouds to obtain a detailed description of the troposphere and in particular of the lower part of the atmosphere where weather systems develop. In order to study the feasibility of observing the Earth's surface from space with an active instrument, a combination of backscatter lidar and multichannel radiometers was flown in space during the Lidar-In-Space Technology Experiment (LITE), during the fall of 1994 [McCormick *et al.*, 1993].

[6] This paper investigates the structure of the MABL in the vicinity of a high-pressure/low-pressure dipole over the remote South Atlantic Ocean (SAO) using a combination of spaceborne and airborne lidar retrievals, satellite imagery and airborne in-situ measurements in conjunction with numerical simulations. Airborne lidar and in situ (dropsondes) observations were acquired from the National Aeronautics and Space Administration (NASA) P-3B aircraft during one selected case of the LITE aircraft correlative measurements, on 15–16 September 1994. The objective of this program was to collect coincident airborne lidar measurements with the LASAL (Large Aperture Scanning Airborne Lidar) system along the space shuttle flight tracks over the Atlantic Ocean. The 15–16 September case was selected as being the only track flown over the remote SAO (Figure 1). The area under scrutiny has been targeted by previous field campaigns such as the Southern African

Regional Science Initiative experiments, i.e., SAFARI-92 [Lindesay *et al.*, 1996] and SAFARI 2000 (R. J. Swap and H. J. Annegarn, Southern African Regional Science Initiative SAFARI 2000: Science Plan, 1999, available from <http://safari.gecp.virginia.edu/>) as well as the Transport and Chemical Evolution over the Atlantic (TRACE-A) experiment [Fishman *et al.*, 1996] which aimed at understanding the processes involved in biomass burning and pollutant transport from an emission source in specific synoptic conditions. Besides the airborne measurements, and with the notable exception of satellite imagery, no other observations were available in this area. Hence the three-dimensional structure of the MABL has been obtained from numerical simulations using the mesoscale non-hydrostatic model Meso-NH [Lafore *et al.*, 1998].

[7] This paper addresses the following questions: (1) What is the atmospheric boundary layer structure in the vicinity of a high-pressure/low-pressure system? (2) What are the consequences on the cloud structure and low level wind field? (3) How well can a mesoscale model simulate such an event?

[8] In section 2, the LITE experiment is presented with a description of the experimental setting and the meteorological situation. Section 3 briefly describes the model used in this study and the modeling strategy for our simulations. In section 4 we discuss cloud cover as well as atmospheric horizontal and vertical structure. The analysis of the atmospheric boundary layer and consequences for atmospheric thermodynamics are also depicted in this section. In section 5, we summarize and conclude.

2. Lidar In-Space Technology Experiment

[9] LITE was flown aboard the space shuttle Discovery in September, 1994 during a nine-day mission to document the

three-dimensional distribution of clouds and aerosols in the atmosphere from an altitude of 260 km [Winker *et al.*, 1996]. LITE collected atmospheric data during ten 4.5 hour periods in a wide range of geographic and atmospheric conditions, including remote areas such as the open ocean, in a very short period of time. Karyampudi *et al.* [1999] have used LITE data to get insights into a conceptual Saharan dust plume model and to examine the evolution of the optical properties undergone by Saharan aerosols across the West Africa and East Atlantic regions. Powell *et al.* [1996] have shown that enhanced aerosol layers were associated with the transport of wind blown dust from the interior of the Sahara Desert across the Atlantic Ocean. Grant *et al.* [1996] have used LITE data to study the features observed in biomass burn plumes over South America, Africa and outflow from Africa. Recently, Stephens *et al.* [2001] introduced a new method to invert the lidar equation for application to spaceborne lidar data using LITE observations.

[10] To validate these data acquired from space, LITE correlative measurement campaigns, involving ground based and airborne measurements, were performed in Italy [Cuomo *et al.*, 1997, 1998], over Europe [European Space Agency (ESA), 1996] and over the Atlantic Ocean [Palm *et al.*, 1998; Schwemmer *et al.*, 1996].

2.1. LITE Aircraft Correlative Measurements Over the Atlantic Ocean

[11] In order to analyze LITE data and study the marine atmospheric boundary layer over the remote Atlantic Ocean, five nighttime underflight missions have been performed with the NASA P3-B aircraft to collect coincident data along the shuttle flight track. The flight trajectories and the dates are shown in Figure 1.

[12] The P3-B was equipped with the LASAL system [Palm *et al.*, 1994], the Radar Ocean Wave Spectrometer (ROWS) system [Vandemark *et al.*, 1994], the NASA/JPL (Jet Propulsion Laboratory) Sea Surface Temperature Radiometer (SSTR) [Hagan, 1988] and the University of Massachusetts Ku-band Scatterometer (KUSCAT) [Carswell *et al.*, 1994]. It also had the capability of dropping sondes. The NASA P-3B LITE correlative missions are further described elsewhere [Palm *et al.*, 1998].

2.2. Synoptic Setting Over the Subtropical SAO

[13] This study focuses on the 15–16 September 1994 mission over the subtropical SAO. This case has been selected among the five missions because it was the only one over the remote SAO. Furthermore, this case was of interest because the elevated cloud cover in the region did not prevent MABL observations by both lidars. Finally, the flight track intersected a frontal area (in the vicinity of a high-pressure/low-pressure dipole) across which the MABL structure varied significantly.

[14] The meteorological situation is presented in Figure 2 based on the ECMWF (European Center for Medium-Range Weather Forecasts) analyses for 15 September at 0000 UTC: mean sea level pressure and surface wind speed (Figure 2a), equivalent potential temperature at 900 hPa level (Figure 2b) and sea surface temperature (SST) (Figure 2c). The P3-B flight track is indicated by thick black lines.

[15] Over the Central SAO, the region of high pressure (i.e., larger than 1020 hPa) extended from 5°S to 35°S, with an anticyclone located off the Brazilian coast, centered on 25°W and 25°S. Above the South American and African continents, the regions of high pressure are located further to the South, roughly between 35°S and 45°S, and 20°S and 45°S, respectively. The position of the high over eastern South Africa was favorable to air mass re-circulation over the African continent which generally leads to enhanced transport of biomass burning particles or/and dust over the ocean [Garstang *et al.*, 1996]. In the eastern part of the SAO (i.e., east of 20°W), the surface pressure distribution was complex and characterized by poleward intrusion of high pressure to the east and equatorward intrusion of low pressure to the west. A surface low (1000 hPa) was centered at 15°W, 45°S.

[16] The dynamics over the SAO also appeared to be very complex. Over the western part of the basin, strong westerlies are observed between 45°S and 55°S off the southern tip of the South American continent. Upon reaching 40°W, the westerlies shift to southwesterlies. The southwesterly flow then split around the surface low, the southern branch turning south and the northern branch merging with the northwesterly flow circulating around the surface high, then turning to the southeast. To the north, southeasterlies were observed across the Atlantic basin. As a result, the flow was southeasterly along the northern portion of the flight track and northwesterly along its southern portion. Low wind speeds were observed between 20°S and 25°S due to the diffuence zone resulting from the stacked position of the surface high and low. The flight track also ran along the eastern edge of the colder air mass moving equatorward, as shown in Figure 2b by the presence of a strong gradient of equivalent potential temperature. Clouds are expected to be observed along this frontal boundary.

[17] Finally, Figure 2c represents the SST provided by the National Center for Environmental Prediction (NCEP) analysis. SST analyses are produced weekly from in-situ (ships, buoys) and satellite observations. The interpolation method is described by Reynolds and Smith [1994]. A zonal gradient of SST disrupted by the Bengala upwelling can be observed. This pattern is likely to influence the MABL structure along the MABL [Rogers, 1989]. The SST issued from Reynolds' climatology yields characteristic spatial and temporal scales of about 2° and 8 days, and cannot resolve small-scale structure in the SST field.

[18] Figure 3 shows the geopotential field and the wind field at 500 hPa issued from ECMWF analyses. A succession of troughs and ridges correlated with the position of surface highs and lows was observed. The southern part of the flight track was under the influence of westerlies, while the northern part was under the influence of a northeasterly flow resulting from the presence of an elevated high positioned on the western African coast. This type of circulation has important implications on the transport of aerosol from biomass burning over Africa.

[19] Horizontal wind, air and dew point temperature profiles as well as the vertical velocity profile issued from ECMWF analyses are shown in Figures 4a and 4b, respectively. The emagram in Figure 4a revealed the MABL to be topped by a stratocumulus layer capped at 850 hPa. The lower inversion near 850 hPa is the trade-wind inversion.

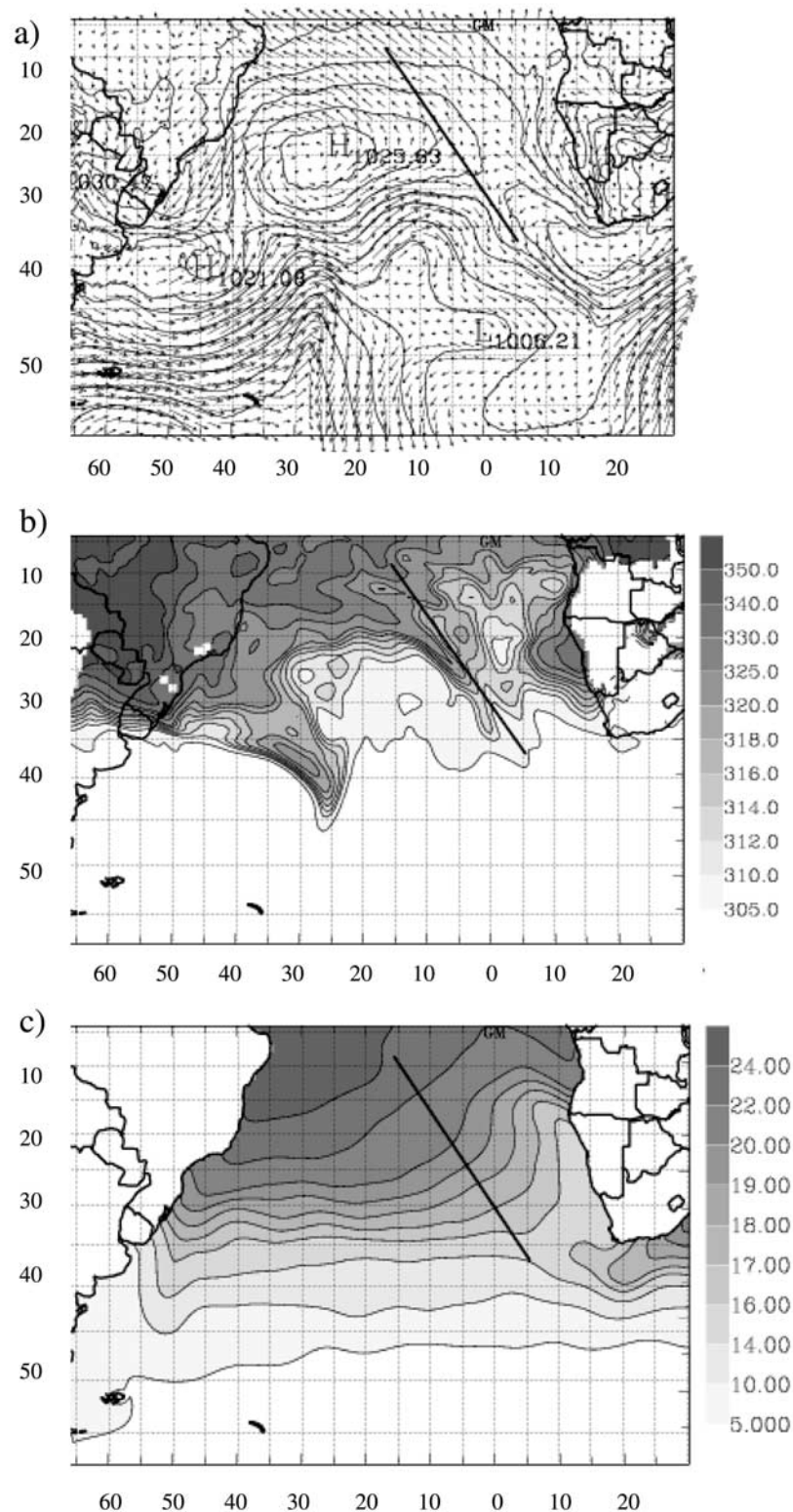


Figure 2. Surface and 900 hPa charts for 0000 UTC on 15 September 1994 extracted from ECMWF analyses: (a) mean sea level pressure with 3 hPa intervals and winds vector at 10 m above sea level, (b) equivalent potential temperature at 900 hPa and (c) sea surface temperature. The black line indicates the P3-B flight track.

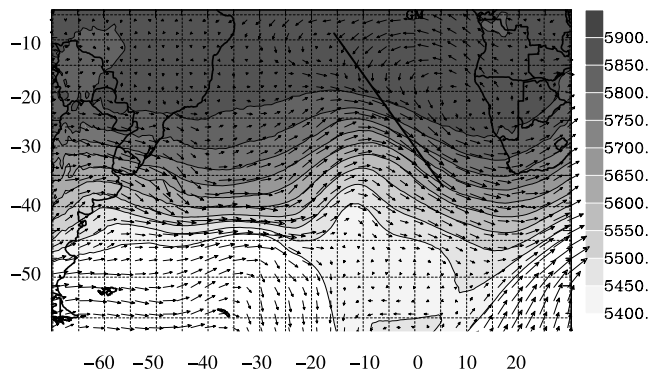


Figure 3. Geopotential height and wind vectors at 500 hPa extracted from ECMWF analyses. The black line indicates the P3-B flight track.

The vertical profiles of temperature and dew point indicate moist tropical air extending up to a height of 2 km above sea level (ASL) (800 hPa). Below this level, the atmosphere was conditionally unstable as shown by the temperature stratification close to the dry adiabatic. The wind shear was small below 700 hPa. Vertical velocities were positive in this layer, as indicated in Figure 4b, due to convergent flow at low levels. Above 850 hPa, the atmosphere was warmer and drier. An inversion at 550 hPa was also observed which was caused by large scale subsidence associated with the Hadley cell's descending branch in the vicinity of 20°S. Subsidence was well marked between 2 and 6 km above sea level (ASL) (Figure 4b). The inversion at 550 hPa was also associated with a large horizontal wind shear (southwesterlies below 550 hPa and easterlies above that height).

[20] The existence of the inversions at 850 and 550 hPa was favorable to the transport of aerosols aloft (e.g., resulting from biomass burning) over large distances.

3. Numerical Simulations

[21] Observations available for this study were essentially acquired along the flight track. To complement these observations, numerical simulations were made using the Meso-NH model to provide the three-dimensional environment necessary for the interpretation of in situ and lidar measurements. After a validation exercise against available observations, Meso-NH model will be used to provide a detailed description of the structure, dynamics and thermodynamics of the atmospheric boundary layer.

3.1. Model Presentation

[22] Numerical simulations have been performed with the mesoscale three-dimensional model Meso-NH developed jointly by Météo-France and the Centre National de la Recherche Scientifique (CNRS). Meso-NH is a non-hydrostatic model able to simulate atmospheric processes from the mesoscale [Mallet *et al.*, 1999] to the scale of large-eddy simulations (LES) [Cuxart *et al.*, 2000]. More details on the model can be found in Lafore *et al.* [1998]. In our study, the following parameterizations have been activated: the ISBA (Interface Sol-Biosphère-Atmosphère) soil scheme [Noilhan and Planton, 1989], the turbulent scheme implemented by Cuxart *et al.* [2000] in a 1D version, the radiative scheme used at ECMWF [Morcrette, 1989], the convection scheme

developed by Bechtold *et al.* [2001] and a microphysical scheme with liquid and ice phases [Pinty and Jabouille, 1999]. Three ice phase are parameterize: pristine ice, snow or aggregates and graupel. Shallow and deep convection have been activated in the simulations. Shallow convection resolves non precipitating clouds with a minimum radius of 50 m and a minimum thickness of 500 m. Deep convection can represent precipitating clouds with a radius and a thickness greater than to 1500 and 3000 m, respectively.

3.2. Modeling Strategy and Initialization

[23] For this simulation, 3 stationary 10-km resolution domains were nested within a 50-km domain using one-way

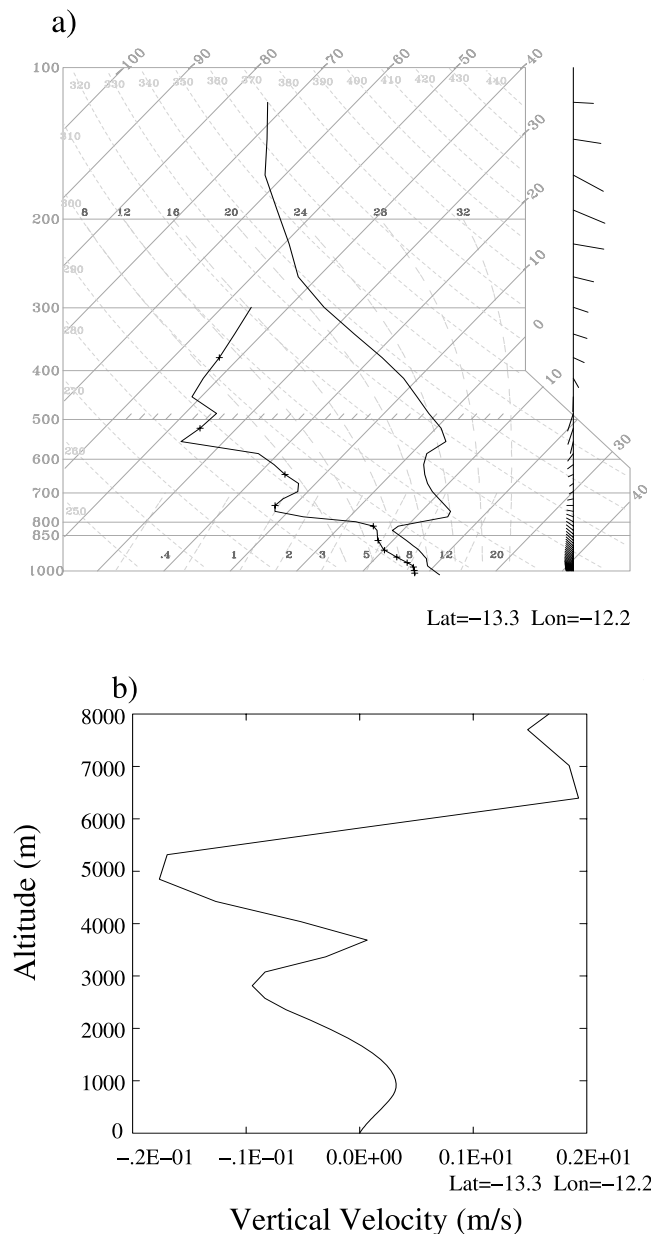


Figure 4. (a) Emagram extracted from the ECMWF analyses, showing vertical profiles of temperature, dew point and horizontal wind at 13.3°S and 12.2°W at 0000 UTC on 15 September 1994, (b) Profile of vertical velocity at the same location.

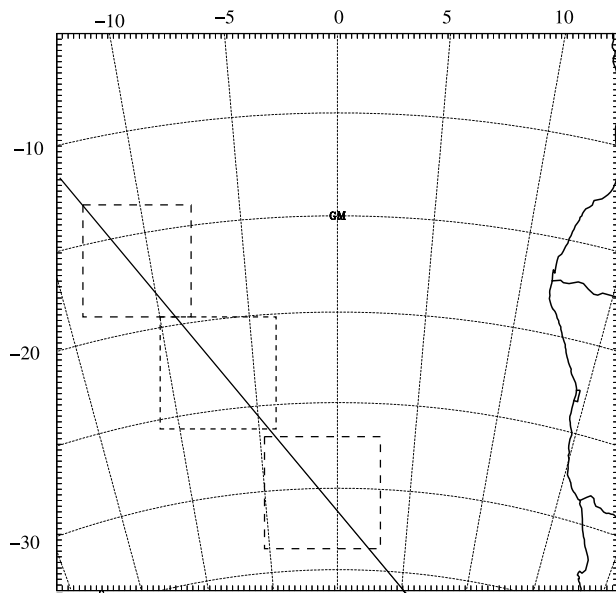


Figure 5. Domains used in nested simulations. The background domain corresponds with the 50 km resolution. The 10 km grid domains are denoted by dashed rectangles. The black line indicates the P3-B flight track.

interfaces [Stein *et al.*, 2000]. The initial fields and the boundary conditions for the 50-km domain were provided by ECMWF analyses available every 6 hours. The 50-km domain is centered at 20°S and 0°W and covers an area of about 200 km × 200 km (compare Figure 5). Simulations were started on 14 September at 1200 UTC and ended at 0300 UTC on 16 September. The 3 10-km domains were positioned so to contain the flight track starting at 1800 UTC on 14 September. The same physical package is used for all simulations. The vertical grid is stretched with a

resolution of 10 m near the ground and 1 km at the top of the model at an altitude of 20 km.

4. Atmospheric Boundary Layer and Cloud Structure in the Subtropical Convergence Zone

4.1. Horizontal Cloud Structure at the Mesoscale

[24] Figure 6 shows a comparison between observed and simulated infrared brightness temperatures at 0000 UTC on 15 September. Meteosat data have been provided by Eumetsat with a spatial resolution of 2.5 km, and interpolated to the model grid. Meso-NH derived brightness temperatures have been obtained using the work of Chaboureaud *et al.* [2000].

[25] Brightness temperatures less than −20°C were observed around 0°W and 30°S, indicating the presence of a cold front. Convective clouds can also be observed offshore from the African coast along the flight track, with temperatures between −25 and 0°C. These clouds were associated with convective activity developing ahead of the cold front. North of these cloud bands, temperatures varying between −15 and 15°C could indicate the presence of cumuliform and stratiform clouds.

[26] The model reproduces the observed cloud band structure associated with the cold front, which spread all the way to the African coast. However, simulated clouds have lower temperature than those observed. This difference may be due to the presence of elevated cloud layers in the simulations and/or caused by an excess in ice condensate mixing ratio in the Meso-NH microphysical scheme. The sensitivity of brightness temperature to ice parameterization has already been evidenced by Chaboureaud *et al.* [2002]. Simulations produced clouds in the vicinity of 20°S (close to where dropsonde measurements were made, indicated in Figure 6 by the black dot). No clouds were observed in the western part of the domain.

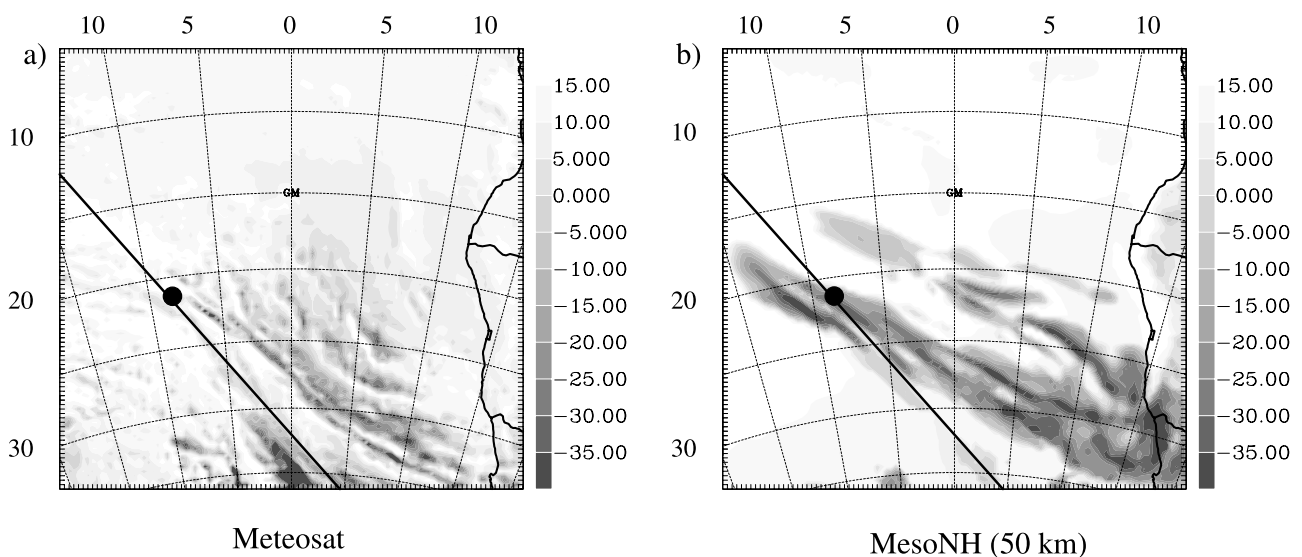


Figure 6. Infrared brightness temperature at 0000 UTC on 15 September 1994 observed by Meteosat (a) and simulated by Meso-NH (b). The black line indicates the P3-B flight track and the black dot indicates the position of dropsonde launch.

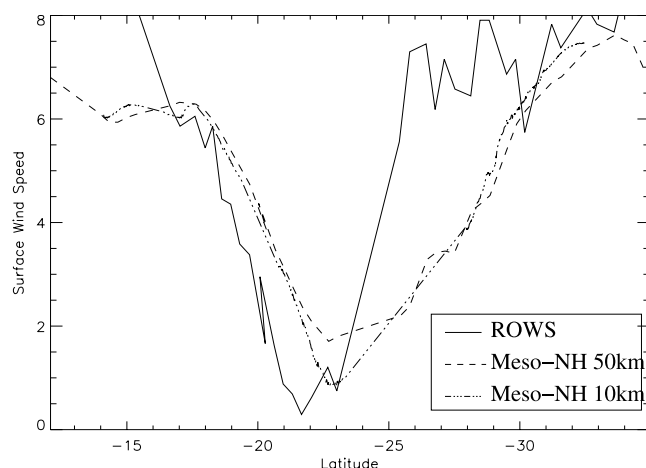


Figure 7. Wind speed at 10 m above sea surface along the P3-B flight track observed by the ROWS system (solid line) as well as simulated by Meso-NH with a 50-km (dotted line) and a 10-km (dot-dashed line) resolution at 0100 UTC on 15 September 1994.

[27] Between the cloud bands to the east and the clear air to the west of the domain, the cloud cover appeared to be broken and may correspond to a region of transition from stratocumulus to cumulus, as warmer waters are more favorable to cumulus formation [Betts and Boers, 1990; Bretherton and Pincus, 1995]. The model cannot reproduce this broken pattern. Chaboureaud and Bechtold [2002] have shown that the quality of the representation of stratiform to shallow cumulus transitions heavily depended on the performances of the turbulent and sub-grid condensation schemes. Due to the coarser resolution of the simulation shown here (50 km), a simplified turbulence scheme without sub-grid condensation was activated, which could explain the discrepancies between model and observations.

4.2. Vertical Structure of the Lower Troposphere

4.2.1. Thermodynamics

[28] Surface wind speed (10 m ASL) measured by the ROWS as well as extracted from the 50-km and 10-km simulations on 15 September 1994 at 0000 UTC are shown in Figure 7. The ROWS showed a large decrease of surface wind speed (from 6 to 1 m s⁻¹) near 22°S. This drop-off was simulated by meso-NH, the best agreement between model and observations being obtained for the 10-km resolution run. However, in both simulations the wind speed minimum was located further south than observed (near 23°S). The 50-km run tends to overestimate the wind speed minimum (2 instead of 1 m s⁻¹). The distance within which wind speeds are less than 6 m s⁻¹ was simulated to be broader by almost 4° of latitude. North of 17°N and south of 30°S, the model also underestimated the wind speeds in both runs.

[29] Vertical profiles of humidity, potential temperature, wind speed and wind direction measured by a dropsonde launched at 0100 UTC on 15 September 1994 in the vicinity of 22.7°S and 6.65°W is shown in Figure 8. Profiles extracted from the model 10-km run at the same time and location are also shown. The location of the dropsonde launch is indicated in Figure 6 by a black dot.

[30] Significant differences are evident between the model and the observations in terms of wind speed and direction (Figures 8a and 8b). The observations suggested southeasterly winds up to 500 m ASL. This was due to the nearby surface high centered on 25°W and 25°S (see Figure 2a). Above 1000 m ASL, westerlies were observed, in accordance with the circulation shown in Figure 3. Only small discrepancies were found between the profiles extracted from the 10-km and 50-km model runs, except near the surface. Generally speaking, the model underestimated the wind speed by as much as 7 m s⁻¹ (Figure 8a), slightly larger differences being obtained for the 10-km run below 1200 m ASL. Below 500 m ASL, the wind direction was correctly reproduced in the 10-km run only. Above that height both simulations suggested winds with a more or less pronounced westerly component, as in the observations. However, between 500 and 3000 m ASL, the southerly component of the simulated flow was too large.

[31] Good agreement was found between the model and the observations in terms of vertical stratification (see the potential temperature profile, Figure 8c). The MABL was observed as a 400 m ASL deep layer on the potential temperature profile. The trade winds inversion was observed at 2000 m ASL to be associated with large potential temperature and humidity gradients (Figures 8c and 8d). Large relative humidity values were observed and simulated below this inversion. Even though the general agreement between observations and simulations was good, two notable discrepancies can be noted. First, in the simulations, relative humidity values in excess of 70% are only seen to be associated with the MABL and the so-called cloud layer below the trade inversion. Observations suggested that relative humidity values in excess of 70% were also present above the MABL. Then, enhanced relative humidity values are seen in the simulations at 5000 m ASL (Figure 8d) but not in the observations. Note that this height also corresponded to the melting level in the model. Below that height, the model will “melt” icy hydrometeors. Hence, the overestimation of relative humidity at 5000 m ASL in the model was likely related to an excess in ice condensate mixing ratio produced by the Meso-NH microphysical scheme.

[32] The origin of the discrepancies between observations and simulations in the lower 2000 m may be due to: (i) the poor quality of the ECMWF analyses over the remote SAO and/or (ii) the representation of turbulent motion in cumulus clouds (entrainment, detrainment) in the model, and more specifically the convective momentum transport.

4.2.2. Vertical Cloud Structure

[33] LITE and LASAL operate in the visible part of the spectrum and use sub-micron aerosols as tracers to document the lower tropospheric structure. Lidar signal is proportional to particle concentration so that lidar derived atmospheric reflectivity is generally observed to be large in regions of the atmosphere characterized by high aerosol concentrations and/or high relative humidities. Hence, ABLs and elevated aerosol plumes can be detected unambiguously from lidar measurements. The signal backscattered by any dense medium (such as clouds or the Earth’s surface) is 1 to 2 orders of magnitude larger than the signal backscattered by particles which implies that the signature

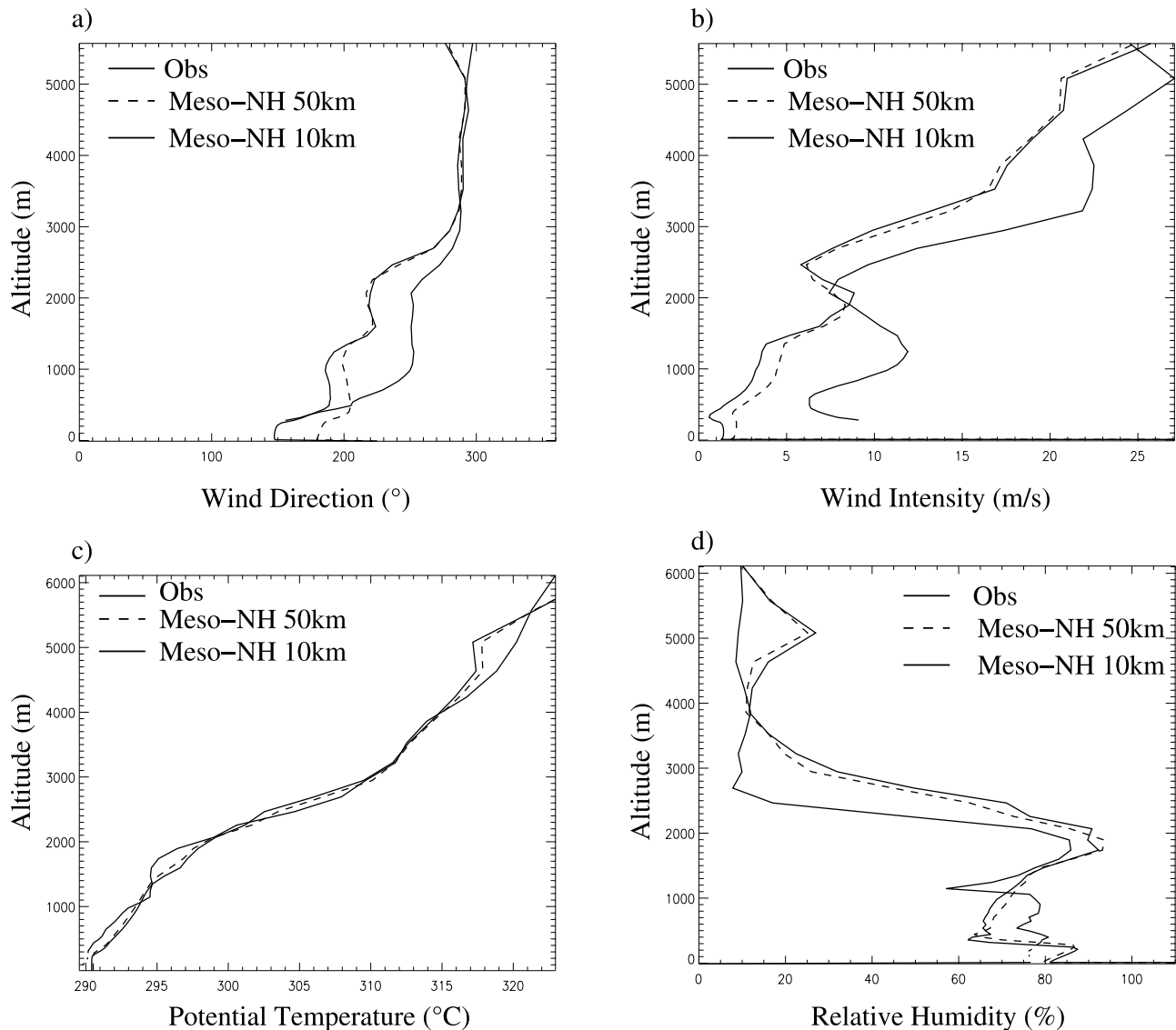


Figure 8. Vertical profiles of wind direction (a), wind speed (b), temperature (c), and relative humidity (d) observed by dropsonde (solid line), and provided by the 50-km (dashed line) and 10-km (dot-dashed line) resolution simulations at 0100 UTC on 15 September 1994 at 22.7°S and 6.65°W.

from aerosol layers can also be segregated from that of clouds.

[34] The two dimensional vertical cross section of lidar reflectivity at 532 nm along the orbit for LITE at 0300 UTC on 15 September is shown in Figure 9a. The lidar reflectivity cross section obtained at 1064 nm from LASAL along the same track between 2200 UTC on 14 September 1994 and 0400 UTC on 15 September 1994 is shown in Figure 9b. The vertical resolution for both systems was 15 m. The horizontal resolution associated with the LITE and LASAL data was originally 700 m and 60 m, respectively. In order to provide meaningful intercomparisons, the horizontal resolution of both data sets was degraded to 7 km.

[35] Between 10°S and 17°S, LITE measurements showed an aerosol laden layer between 2 and 4 km ASL. According to the circulation pattern shown in Figure 3, this layer is likely to be associated with biomass burning transport from South Africa, which is very important during this

season [Swap *et al.*, 1996]. The vertical extent of the aerosol plume appeared to be limited by the trade wind inversion below and the large-scale subsidence inversion above. Below the aerosol plume, a rather solid cloud layer deck was observed, the top of the cloud layer being located around 1.5 km ASL. South of 15°S a transition from solid to broken cloud deck was observed. Between 15°S and 23°S, a succession of solid cloud decks, broken cloud decks and clear air was observed. The height of the cloud layer top remained approximately constant in that region. Consistent with the dropsonde measurements (Figure 4a), the atmosphere was dry (cloud free) above the trade wind inversion to the north of 22°S.

[36] Further to the south, multiple cloud layers were observed. Between 23°S and 28°S, cumulus towers were seen to reach heights of 2 to 3 km, while the top of the fairly solid cloud layer remained relatively unchanged in altitude. South of 28°S, the cloud top height appeared to increase

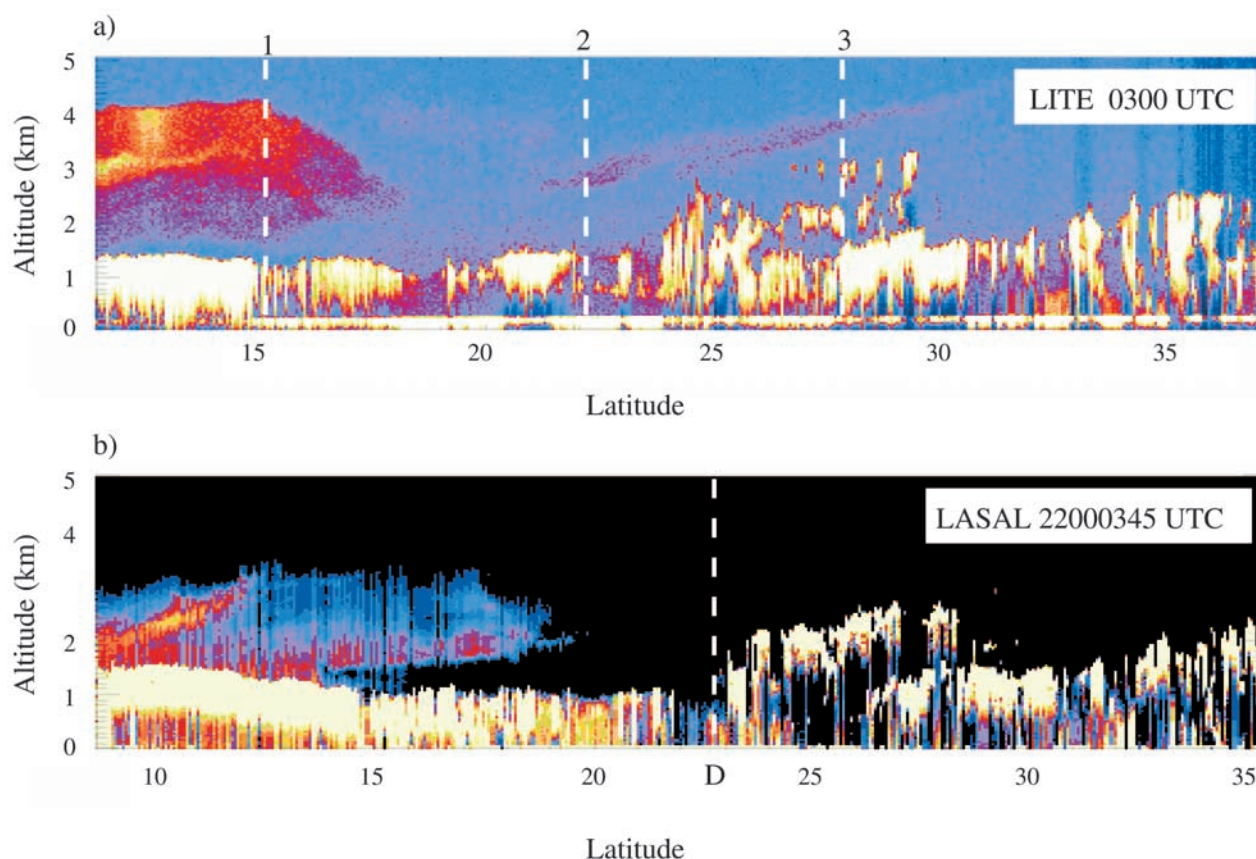


Figure 9. False color image of 2D vertical cross section of lidar reflectivity along the flight track for LITE system (a) and LASAL system (b). In panel (a), the MABL and the elevated aerosol plume appear in red, while the free troposphere appears in blue. High reflectivity values associated with clouds are shown in white. Note that the surface echo also appears in white. Finally, the low reflectivity values observed below the clouds (blue) are caused by the extinction undergone by the laser beam as it penetrates the clouds. No meaningful interpretation of the data below the clouds can be made. In panel (b), the free troposphere appears in black and the MABL and aerosol plume in blue/red. The vertical dotted lines indicate the position of profiles presented in Figure 10 in figure a) and the position of the dropsonde measurements in figure b).

with latitude over colder ocean water (compare Figure 2c). South of 35°S, there was evidence of decoupling between the elevated cloud layer and cumulus clouds below, the latter reaching 1 km ASL. *Betts and Boers* [1990] and *Bretherton and Pincus* [1995] have suggested that cold waters are favorable to the formation of stratocumulus, often present over the eastern border of the oceans, while warmer waters favored the development of cumulus clouds. This was not observed here. The reason for this is believed to be related to the fact that the LITE orbit in that region was in the vicinity of (i.e., running parallel to) a surface front (Figure 2b). The cold air intrusion in that region may have provided the uplift observed in Figure 9a.

[37] Figure 9b also shows that the LASAL and LITE reflectivity cross-sections were in good agreement, despite the speed difference of their respective platforms. The same general characteristics were observed: elevated aerosol plume, multilayered cloud structure south of 23°S, sloping cloud layer top height with increasing latitude. The small differences observed between the LITE and LASAL measurements are related to the fact that LITE provided the

measurements shown in Figure 9a quasi-instantaneously while it took several hours of LASAL data to create a comparable cross-section. The LITE measurements were exactly coincident with those of LASAL at about 32.5°S on the flight track.

4.2.3. Marine Atmospheric Boundary Layer

[38] In order to study the dynamics of the MABL along the P-3B flight track, an objective algorithm to detect the top of the MABL on the LASAL/LITE data was used. Wherever available, these heights will be compared to those retrieved from simulations. In places where LASAL could not “see” the MABL because of overlying clouds, we shall use MABL top heights obtained from the simulations to “fill in” the gaps.

[39] The MABL top retrieval algorithm used for LASAL and LITE measurements has been developed by *Flamant et al.* [1997] for yet another airborne lidar. This algorithm can also be used to determine cloud top height from nadir pointing lidar measurements. It is based on the derivative of the range-squared corrected signal (RSCS) and two threshold values (one for clear atmospheric boundary layer

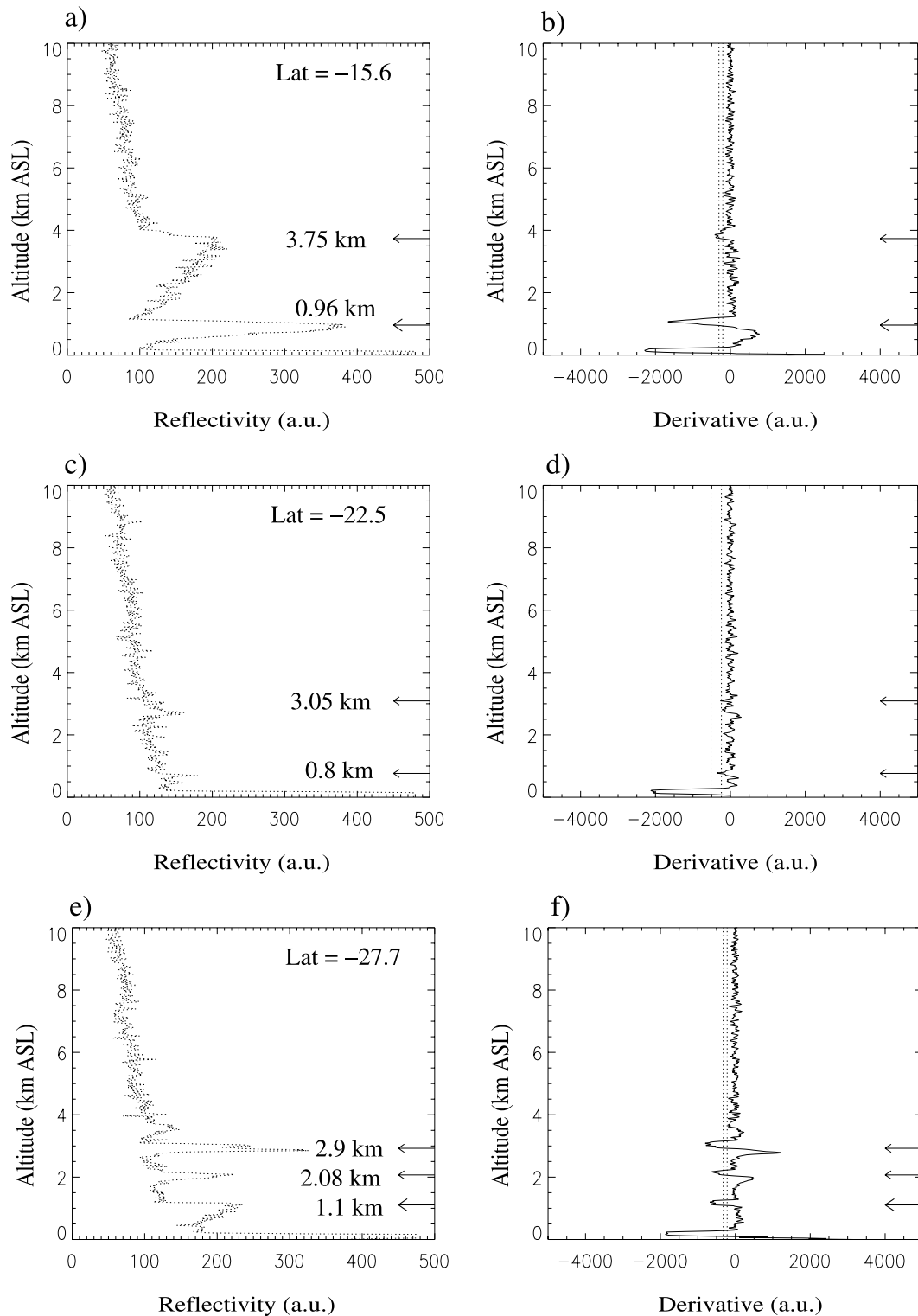


Figure 10. Profiles of lidar range-squared corrected signal (panels a, c and e) acquired by LITE. The locations of these profiles are indicated by dotted lines noted 1, 2 and 3, respectively, in Figure 9. The corresponding profiles of lidar range-squared corrected signal derivative with respect to height are given in panels b, d and f.

and elevated aerosol layers and one for cloud top detection). The MABL top height is defined as the lowest point on the RSCS derivative profile for which the derivative is smaller than the corresponding threshold. Examples of MABL/

aerosol layer/cloud layer top height retrievals are given in Figure 10 for LITE data. The locations of these profiles are indicated in the two-dimensional cross section of lidar reflectivity (compare Figure 9). The three profiles were

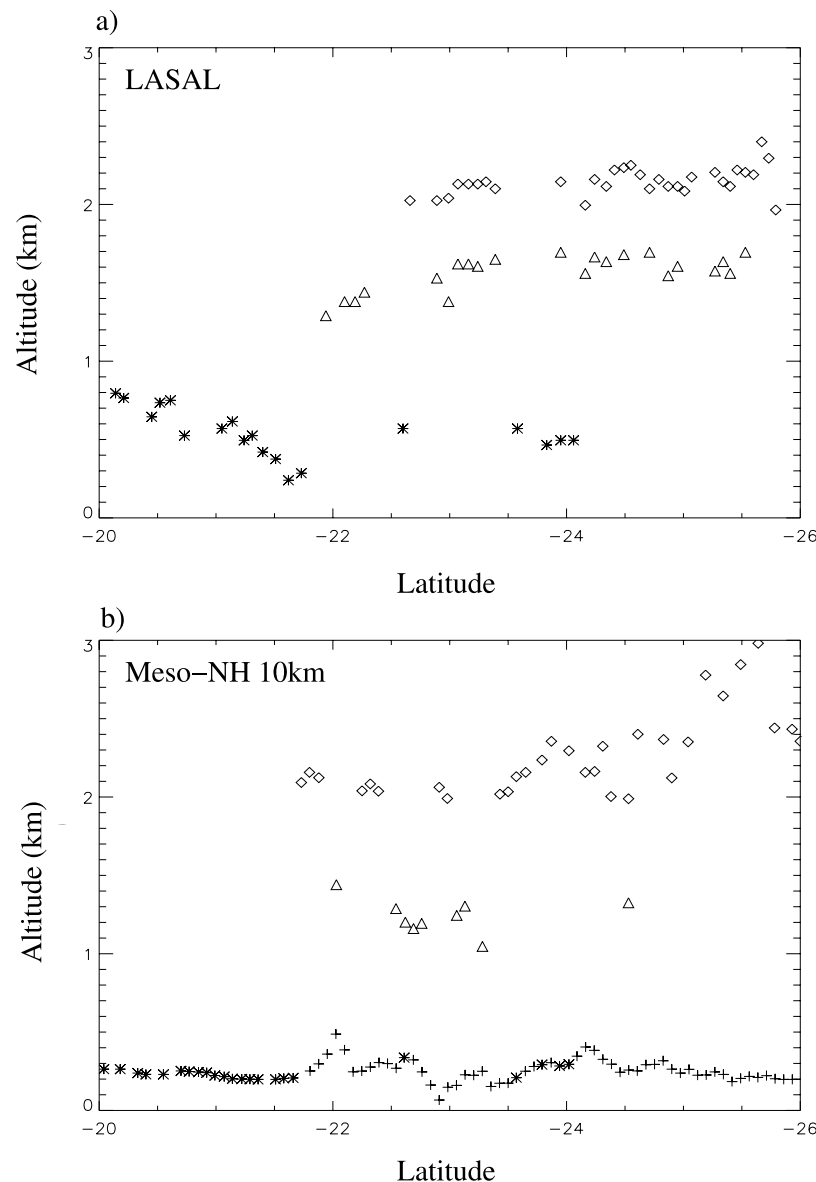


Figure 11. MABL top height (clear air only, *) and cloud top height (Δ , \diamond) observed by LASAL along the flight track (a) and simulated by Meso-NH with a 10-km resolution for the 15 September at 0100 UTC (b). The symbols (+) represent model-derived MABL height below cloud layers (i.e., not seen by lidar).

chosen to illustrate different regions observed along the track. In the first profile (Figures 10a and 10b), the algorithm detects the top of aerosol plume (3.75 km ASL) and the cloud layer top at 0.96 km ASL. We can see on these two profiles that the reflectivity associated with clouds is higher than that associated with the aerosol plume. The high reflectivities associated with the aerosol plume with respect to the ambient clearer air was caused by the enhanced concentrations and size of the advected aerosols which far exceed those generally found for background natural aerosols over the open ocean. The even stronger return associated with clouds is because the cloud droplets provide much bigger targets than submicron size aerosols (to which the lidars are sensitive) and backscatter light more efficiently. The strong decrease in reflectivity generally observed below clouds is related to the extinction of the laser beam. The

second example shows a profile located in a clear region (Figures 10c and 10d). Reflectivity transitions (hence aerosol layer tops) near 3.5 km ASL and around 0.8 km ASL can be detected unambiguously. The latter corresponds to the MABL top even though the signature is not very pronounced. Indeed the lidar-derived atmospheric reflectivity is generally observed to be large in regions capped by a temperature inversion because particles are trapped below the inversion in the MABL. Above this inversion, the particle concentration diminishes so the lidar signal will decrease rapidly. The third example shows a multilayered cloud structure with layer tops near 2.9 km, 2.08 km and 1.1 km ASL. In summary, the algorithm developed by *Flamant et al.* [1997] has the capability to distinguish MABL from elevated aerosol layers as well as MABL (or elevated aerosol layers) from clouds.

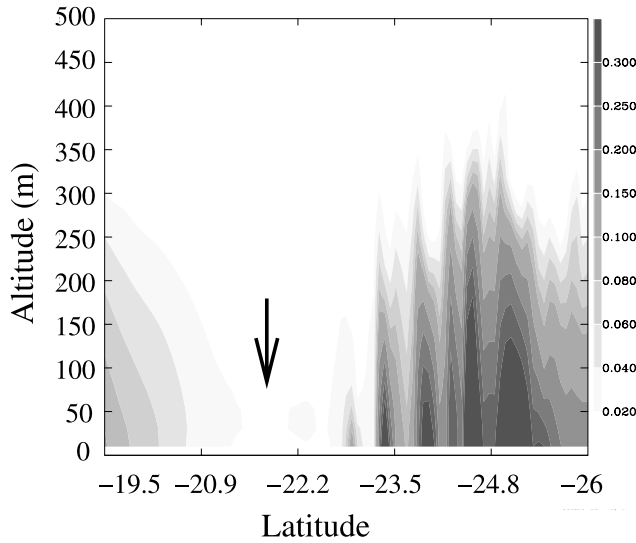


Figure 12. Vertical cross section of the modeled turbulent kinetic energy along the P3-B flight track at 0000 UTC on 15 September 1994. The black arrow indicates the position of the wind minimum.

[40] The latitudinal evolution of the MABL top height and cloud layers top height derived from LASAL measurements has been analyzed in the relatively cloud free portion of the P-3B flight track, between 20° and 26°S (Figure 11a). Two cloud layers were observed on that portion of the track, at approximately 1.6 km and 2.2 km ASL. Note that the behaviour of the boundary layer top (when detected) bears resemblance to that of the surface wind speed (Figure 7), i.e., it is characterized by an important “collapse” of 600 m (between 800 and 200 m ASL) in the vicinity of 22°S. The MABL top height and the cloud layer top heights derived from the Meso-NH 10-km simulation on the same portion of the flight track are in Figure 11b. The top of the MABL in the simulation model is defined as the height where the turbulent kinetic energy (TKE) becomes smaller than a threshold value (25% of the maximum TKE on a given TKE profile) [Flamant *et al.*, 2001]. The top of the cloud layers are defined using a threshold on the total water mixing ratio profiles. In Figure 11b, the model retrievals that were coincident MABL top height observations have been plotted as asterisks. The higher cloud layer was simulated in the right position, both in terms of altitude and latitude. The altitude of the lower cloud layer was found to be underestimated in the model. Moreover, it was not found to be as “solid” as the layer observed with LASAL. Finally, the largest discrepancies were found for the MABL top height. In the model, the MABL top height was relatively constant (300 and 400 m ASL), whereas it was observed to vary substantially in the LASAL data (between 200 and 800 m ASL). The origin of the discrepancies between observations and simulations may be due to: (i) the poor quality of the ECMWF analyses over the remote SAO and/or (ii) the representation of turbulent motion in cumulus clouds (entrainment, detrainment) in the model, and more specifically the convective momentum transport.

[41] The MABL “collapse” near 22°S was also less marked in the simulation (300 to 200 m ASL versus 800

to 200 m ASL in the observations). However, TKE along the P-3B flight track on 15 September 1994 at 0000 UTC (Figure 12), exhibited a large decrease around 22°S. This minimum of TKE (indicated in Figure 12 by a black arrow) coincided with the wind speed and MABL top height decrease observed with ROWS (Figure 7) and LASAL (Figure 11), respectively. The MABL top for the model being diagnosed from the TKE profile, a low MABL top height should be obtained in the region where the TKE was very small. We believe that in Figure 11b, the “collapse” of the MABL was underestimated because the model-derived MABL heights had to be interpolated to match the LASAL sampling along the flight track.

[42] In order to understand the peculiar structure of the MABL in this region, we have investigated the variation of the TKE budget along the flight track. The evolution of the TKE in the model reads

$$\frac{\partial e}{\partial t} = -\frac{1}{\rho_{ref}} \frac{\partial}{\partial x_k} \left(\rho_{ref} \overline{u_k e} \right) - \overline{u_i' u_k'} \frac{\partial \overline{u_i}}{\partial x_k} + \frac{g}{\theta_{vref}} \delta_{i3} \overline{u_i' \theta_v'} - \frac{1}{\rho_{ref}} \frac{\partial}{\partial x_j} \left(-C_e \rho_{ref} L e^{1/2} \right) \frac{\partial e}{\partial x_j} - C_\epsilon \frac{e^{3/2}}{L} \quad (1)$$

[43] Here (u, v, w) are the three components of the wind, primes ($'$) denote turbulent components, u_i is the i -component of the wind, θ_v is the virtual temperature, θ_{vref} and ρ_{ref} are the reference temperature and density profiles, respectively, and are specified once and for all. L is the mixing length, g is the acceleration due to gravity, δ_{ij} is the Kronecker delta symbol and C_e and C_ϵ are closure constants. The balance of TKE is maintained by: TKE transport, shear production, buoyancy production, diffusion and dissipation. Figure 13 shows a vertical cross section along the flight track at 0000 UTC on 15 September 1994 of the four principal terms calculated by the model: shear production (Figure 13a), buoyancy production (Figure 13b), TKE transport (Figure 13c) and dissipation (Figure 13d). The diffusion term has been neglected. The location of the minimum of TKE near 22°S corresponds to a quasi-null contribution by each of the terms. This can be explained by the peculiar location of the region under scrutiny. Indeed this area was characterized by very weak horizontal winds (Figure 2a) because it was located east of a diffluence zone caused by strong anticyclonic and cyclonic circulations. This area was also influenced by subsidence in altitude (compare Figure 4b). As shown in Figure 11, this region was cloud free, so that it is likely that vertical motion was inhibited, therefore not enabling the MABL to develop.

5. Conclusion

[44] In this paper, we have presented a study of the MABL structure over the subtropical SAO using both observations and numerical simulations. Observations were provided by spatial and airborne lidars, a ROWS and a dropsondes system. The selected case was the 15 September 1994 case of the LITE experiment during which aircraft underflights were undertaken along the ground track of the Space Shuttle.

[45] The dynamics associated with this case have been shown to be complex and strongly modulated the MABL

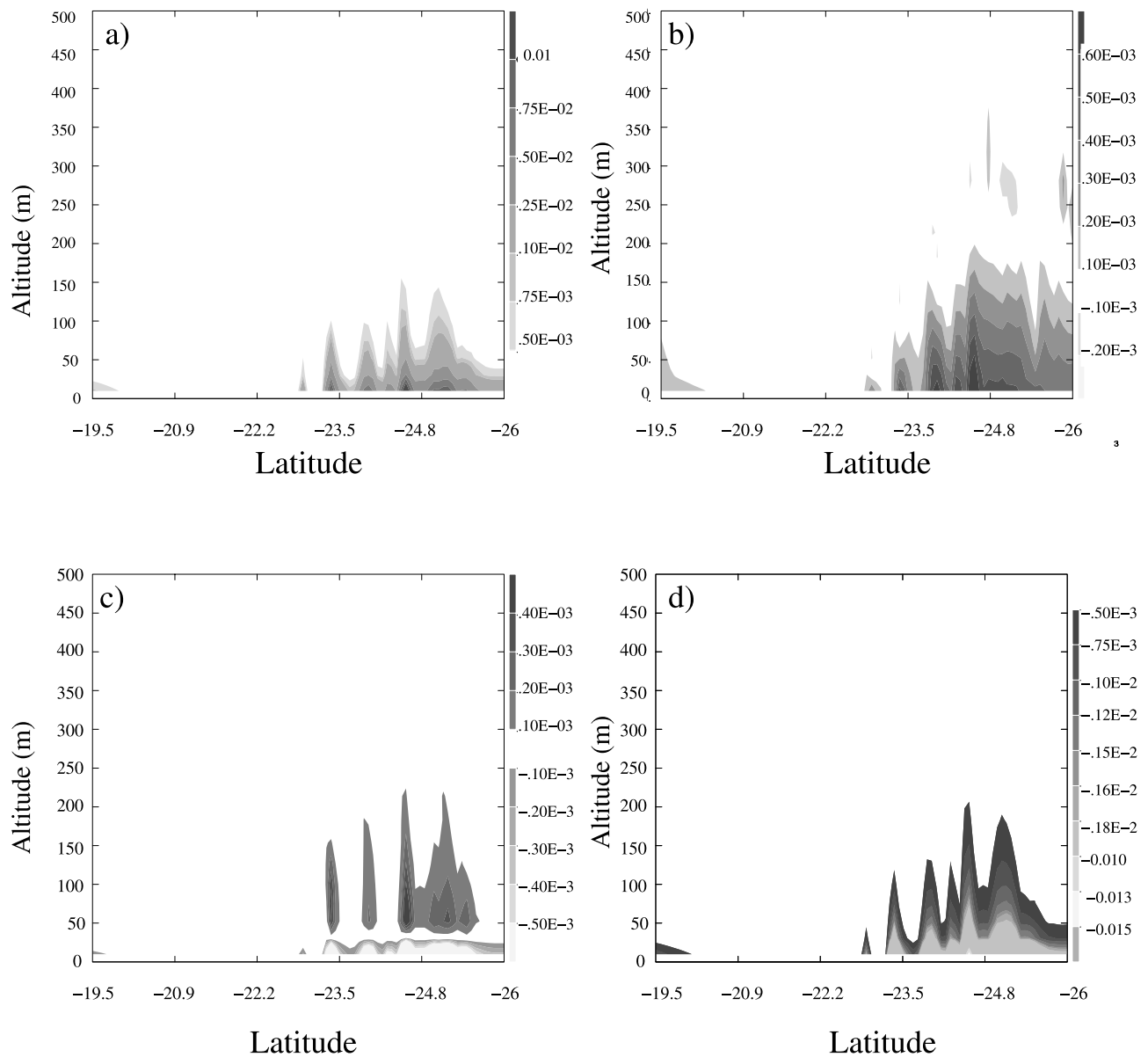


Figure 13. Vertical cross section of the modeled shear production term (a), buoyancy production term (b), TKE advection term (c), and dissipation term (d) along the P3-B flight track at 0000 UTC on 15 September 1994.

structure. The central part of the flight track was simultaneously under the influence of a high/low pressure system over the ocean, the trade winds, a strong north-south gradient in the SST field and subsiding motion associated with the Hadley cell.

[46] Lidar measurements revealed the vertical structure of the atmosphere to be a series of stratocumulus/cumulus/clear air transitions, with sometimes multiple cloud layers. High resolution numerical simulations of this case have been carried out with the Meso-NH model to complement lidar and in situ based investigations of the MABL in the vicinity of the high pressure/low pressure dipole along the flight track. In this region, the structure of the MABL observed by lidar was mostly due to the weak winds which lead to weak

turbulence which in turn inhibited the vertical development of the MABL.

[47] Future work will be focused on the improvement of the turbulence scheme in the model for a more realistic representation of turbulent flux, important for the reproduction of a local dynamics and of the stratocumulus to cumulus transition associated with the deepening of the MABL.

[48] The methodologies and the techniques developed for this study will be applied to lidar data acquired from future planned orbiting lidar systems such as GLAS (Geoscience Laser Altimeter System), scheduled to launch in early 2003, and CALIPSO (Cloud Aerosol Lidar and Infrared Pathfinder Satellite Observation). CALIPSO will be combined with a wide-field visible light camera and a three-color

infrared imaging radiometer and is expected to be launched in April 2004.

[49] **Acknowledgments.** The authors would like to thank Ionela Musat and Geneviève Sèze for providing Meteosat data and D. Vandemark for the ROWS data. They would also like to thank the two anonymous reviewers for comments and suggestions that led to a significant improvement of this paper. This study has been funded by the Centre National de la Recherche Scientifique (CNRS) and by the Centre National d'Etudes Spatiales (CNES). Computer resources were provided by IDRIS (Institut du Développement et des Ressources en Informatique Scientifique), Palaiseau, France, under project 011397-CP1.

References

- Albrecht, B. A., C. S. Bretherton, D. Johnson, W. H. Schubert, and A. S. Frisch, The Atlantic Stratocumulus Transition Experiment, *Bull. Am. Meteorol. Soc.*, **76**, 889–903, 1995.
- Bechtold, P., E. Bazile, F. Guichard, P. Mascart, and E. Richard, A mass flux convection scheme for regional and global models, *Q. J. R. Meteorol. Soc.*, **127**, 869–886, 2001.
- Betts, A., and R. Boers, A cloudiness transition in a marine boundary layer, *J. Atmos. Sci.*, **47**, 1480–1497, 1990.
- Bretherton, C., and R. Pincus, Cloudiness and marine boundary layer dynamics in the ASTEX Lagrangian experiments, part I, Synoptic setting and vertical structure, *J. Atmos. Sci.*, **52**, 2707–2723, 1995.
- Carswell, J., S. Carson, R. McIntosh, F. Li, G. Neumann, D. McGlaughlin, J. Wilkerson, P. Black, and S. Nghiem, Airborne scatterometers: Investigating ocean backscatter under low and high-wind conditions, *Proc. IEEE*, **82**, 1835–1860, 1994.
- Chaboureaud, J. P., and P. Bechtold, A simple cloud parameterization derived from cloud resolving model data: Diagnostic and pronostic applications, *J. Atmos. Sci.*, **59**, 2362–2372, 2002.
- Chaboureaud, J. P., J. P. Cammas, P. Mascart, J. P. Pinty, C. Claud, R. Roca, and J. J. Morcrette, Evaluation of a cloud system life-cycle simulated by Meso-NH during FASTEX using METEOSAT radiances and TOVS-31 cloud retrieval, *Q. J. R. Meteorol. Soc.*, **126**, 1735–1750, 2000.
- Chaboureaud, J. P., J. P. Cammas, P. Mascart, J. P. Pinty, and J. P. Lafore, Mesoscale model cloud scheme assessment using satellite observations, *J. Geophys. Res.*, **107**(D16), 4301, doi:10.1029/2001JD000714, 2002.
- Cox, S. K., D. S. Mc Dougall, D. A. Randall, and R. A. Schiffer, FIRE: The First ISCCP Regional Experiment, *Bull. Am. Meteorol. Soc.*, **68**, 114–118, 1987.
- Cuomo, V., et al., The LITE correlative measurements campaign in southern Italy: Preliminary results, *Appl. Phys. B*, **64**, 553–559, 1997.
- Cuomo, V., P. Di Girolamo, G. Pappalardo, N. Spinelli, V. Berardi, M. Armenante, and M. P. McCormick, Lidar In-Space Technology Experiment correlative measurements by lidar in Potenza, southern Italy, *J. Geophys. Res.*, **103**, 11,455–11,464, 1998.
- Cuxart, J., P. Bougeault, and J. L. Redelsperger, A turbulence scheme allowing for mesoscale and large-eddy simulations, *Q. J. R. Meteorol. Soc.*, **126**, 1–30, 2000.
- De Roode, S., and P. Dyunkerke, Observed Lagrangian transition of stratocumulus into cumulus during ASTEX: Mean state and turbulence structure, *J. Atmos. Sci.*, **54**, 2157–2173, 1997.
- European Space Agency (ESA), ELITE-94: The European 'LITE' Correlative Measurement Campaign, *ESA WPP-107*, 110 pp., Paris, 1996.
- Fishman, J., J. M. Hoell Jr., R. D. Bendura, R. J. McNeal, and V. Kirchhoff, NASA GTE TRACE A experiment (September–October 1992): Overview, *J. Geophys. Res.*, **101**, 23,865–23,880, 1996.
- Flamant, C., J. Pelon, P. H. Flamant, and P. Durand, Lidar determination of the Entrainment Zone thickness at the top of the unstable marine atmospheric, *Boundary Layer Meteorol.*, **83**, 247–284, 1997.
- Flamant, C., V. Trouillet, P. Chazette, and J. Pelon, Wind speed dependence of atmospheric boundary layer optical properties and ocean surface reflectance as observed by backscatter lidar, *J. Geophys. Res.*, **103**, 25,137–25,158, 1998.
- Flamant, C., M. Georgelin, L. Menut, J. Pelon, and P. Bougeault, The atmospheric boundary-layer structure within a cold air outbreak, *Boundary Layer Meteorol.*, **99**, 85–103, 2001.
- Garstang, M., P. D. Tyson, R. Swap, M. Edwards, P. Kallberg, and J. A. Lindesay, Horizontal and vertical transport of air over southern Africa, *J. Geophys. Res.*, **101**, 23,721–23,736, 1996.
- Grant, W. B., E. V. Browell, C. F. Butler, and G. D. Nowicki, LITE measurements of biomass burning aerosols and comparisons with correlative airborne lidar measurements of multiple scattering in the planetary boundary layer, in *18th International Laser Radar Conference*, edited by A. Ansmann et al., pp. 153–156, Springer-Verlag, New York, 1996.
- Grenier, H., and C. S. Bretherton, A moist PBL parameterization for large-scale models and its application to subtropical cloud-topped marine boundary layers, *Mon. Weather Rev.*, **129**, 357–377, 2001.
- Hagan, D., The profile of upwelling 11-micron radiance through the atmospheric boundary layer overlying the ocean, *J. Geophys. Res.*, **93**, 5294–5302, 1988.
- Karyampudi, V. M., et al., Validation of the Saharan dust plume conceptual model using lidar, Meteosat and ECMWF data, *Bull. Am. Meteorol. Soc.*, **80**, 1045–1075, 1999.
- Lafore, J. P., et al., The Meso-NH atmospheric simulation system. I: Adiabatic formulation and control simulations, *Ann. Geophys.*, **16**, 90–109, 1998.
- Lindesay, J. A., M. O. Andreae, J. G. Goldammer, G. Harris, H. J. Anegarn, M. Garstang, R. J. Scholes, and B. W. Van Wilgen, International Geosphere-Biosphere Programme/International Global Atmospheric Chemistry SAFARI-92 field experiment: Background and overview, *J. Geophys. Res.*, **101**, 23,521–23,530, 1996.
- Mallet, I., J. P. Cammas, P. Mascart, and P. Bechtold, Effects of cloud diabatic heating on the early development of the FASTEX IOP17 cyclone, *Q. J. R. Meteorol. Soc.*, **125**, 3439–3467, 1999.
- McCormick, M., et al., Science investigations planned for the Lidar In-Space Technology Experiment (LITE), *Bull. Am. Meteorol. Soc.*, **74**, 205–213, 1993.
- Morcrette, J. J., Description of the radiation scheme in the ECMWF model, *ECMWF Tech. Memo. 165*, Eur. Cent. for Medium-Range Weather Forecasts, Reading, England, 1989.
- Noilhan, J., and S. Planton, A simple parameterization of land surface processes for meteorological models, *Mon. Weather Rev.*, **117**, 536–549, 1989.
- Palm, S. P., S. H. Melfi, and D. L. Carter, New airborne scanning lidar system: Applications for atmospheric remote sensing, *Appl. Opt.*, **33**, 5674–5681, 1994.
- Palm, S. P., D. Hagan, G. Schwemmer, and S. H. Melfi, Inference of marine atmospheric structure using airborne lidar and infrared radiometer data, *J. Appl. Meteorol.*, **37**, 308–324, 1998.
- Pinty, J. P. and P. Jabouille, A mixed-phase cloud parameterization for use in mesoscale non-hydrostatic model: Simulation of a squall line and of orographic precipitations, paper presented at Conference of Cloud Physics, Am. Meteorol. Soc., Everett, Wash., Aug. 1999.
- Powell, K. A., C. R. Trepte, and G. S. Kent, Observations of Saharan dust by LITE, in *18th International Laser Radar Conference*, edited by A. Ansmann et al., pp. 149–152, Springer-Verlag, New York, 1996.
- Reynolds, R. W., and T. M. Smith, Improved global SST analyses, *J. Clim.*, **7**, 929–948, 1994.
- Rogers, D. P., marine boundary layer in the vicinity of an ocean front, *J. Atmos. Sci.*, **46**, 13,2044–13,2062, 1989.
- Schwemmer, G., S. P. Palm, S. H. Melfi, and K. D. Evans, Retrieval of atmospheric boundary layer parameters from LITE and LASAL, in *18th International Laser Radar Conference*, edited by A. Ansmann et al., pp. 161–164, Springer-Verlag, New York, 1996.
- Stein, J., E. Richard, J. P. Lafore, J. P. Pinty, N. Asencio, and S. Cosma, High-resolution non-hydrostatic simulations of flash-flood episodes with grid-nesting and ice-phased parameterization, *Meteorol. Atmos. Phys.*, **72**, 203–221, 2000.
- Stephens, G. L., R. J. Engelen, M. Vaughan, and T. L. Anderson, Toward retrieving properties of the tenuous atmosphere using space-based lidar measurements, *J. Geophys. Res.*, **106**, 28,143–28,158, 2001.
- Swap, R. J., M. Garstang, S. A. Macko, P. D. Tyson, W. Maenhaut, P. Artaxo, P. Kallberg, and R. Talbot, The long range transport of southern African aerosols to the tropical South Atlantic, *J. Geophys. Res.*, **101**, 23,777–23,792, 1996.
- Vandemark, D., F. Jackson, E. Walsh, and B. Chapron, Airborne radar measurements of ocean wave spectra and wind speed during the Grand Banks ERS-1 wave experiment, *Atmos. Ocean*, **32**, 143–178, 1994.
- Winker, D. M., R. H. Couch, and M. P. McCormick, An overview of LITE: NASA's Lidar In-Space Technology Experiment, *Proc. IEEE*, **84**, 164–180, 1996.

S. Cosma-Averseng, C. Flamant, and J. Pelon, Service d'Aéronomie, Université Pierre et Marie Curie, Boite 102, 4 place Jussieu, 75252 Paris Cedex, France. (cosma@aero.jussieu.fr; cyf@aero.jussieu.fr; jpe@aero.jussieu.fr)

S. P. Palm, Science Systems and Applications, Inc., 10210 Greenbelt Road, Suite 600, Lanham, MD 20706, USA. (spp@virl.gsfc.nasa.gov)

G. K. Schwemmer, Laboratory for Atmospheres, NASA Goddard Space Flight Center, Greenbelt, MD 20771, USA. (geary.k.schwemmer@nasa.gov)